PNAS RESEARCH ARTICLE | DEVELOPMENTAL BIOLOGY

Atf7ip and Setdb1 interaction orchestrates the hematopoietic stem and progenitor cell state with diverse lineage differentiation

Jiaxin Wu[a,1], Juan Li[a,1], Kang Chen[b,1], Guolong Liu[a,1], Yating Zhou[a], Wenqi Chen[a], Xiangzhan Zhu[a], Terri T. Ni[a], Bianhong Zhang[a], Daqing Jin[a], Dali Li[a], Lan Kang[b], Yuxuan Wu[a], Ping Zhu[c], Peng Xie[d,2], and Tao P. Zhong[a,2]

Edited by Janet Rossant, Gairdner Foundation, Toronto, Canada; received June 1, 2022; accepted November 21, 2022

Hematopoietic stem and progenitor cells (HSPCs) are a heterogeneous group of cells with expansion, differentiation, and repopulation capacities. How HSPCs orchestrate the stemness state with diverse lineage differentiation at steady condition or acute stress remains largely unknown. Here, we show that zebrafish mutants that are deficient in an epigenetic regulator Atf7ip or Setdb1 methyltransferase undergo excessive myeloid differentiation with impaired HSPC expansion, manifesting a decline in T cells and erythroid lineage. We find that Atf7ip regulates hematopoiesis through Setdb1-mediated H3K9me3 modification and chromatin remodeling. During hematopoiesis, the interaction of Atf7ip and Setdb1 triggers H3K9me3 depositions in hematopoietic regulatory genes including *cebpβ* and *cdkn1a*, preventing HSPCs from loss of expansion and premature differentiation into myeloid lineage. Concomitantly, loss of Atf7ip or Setdb1 derepresses retrotransposons that instigate the viral sensor Mda5/Rig-I like receptor (RLR) signaling, leading to stress-driven myelopoiesis and inflammation. We find that ATF7IP or SETDB1 depletion represses human leukemic cell growth and induces myeloid differentiation with retrotransposon-triggered inflammation. These findings establish that Atf7ip/Setdb1-mediated H3K9me3 deposition constitutes a genome-wide checkpoint that impedes the myeloid potential and maintains HSPC stemness for diverse blood cell production, providing unique insights into potential intervention in hematological malignancy.

HSPC | epigenetics | myeloid differentiation | retrotransposon | leukemia

Significance

The diverse and balanced differentiation of HSPCs is essential for sustaining the peripheral blood homeostasis. In this study, we employ genome-wide profiling analyses combined with time-lapse imaging and functional assays to characterize developing HSPCs. First, we analyze zebrafish mutants and elucidate the interaction of Atf7ip and Setdb1 in controlling definitive hematopoiesis. We then dissect epigenetic regulations, identifying H3K9me3 deposition mediated by Atf7ip and Setdb1 as a key epigenetic checkpoint that coordinates the HSPC stemness state with hematopoietic differentiation. Atf7ip and Setdb1 interaction is also required for silencing retroelements to prevent RLR-mediated inflammation and biased myelopoiesis. Finally, we uncover that ATF7IP/SETDB1 depletion suppresses leukemic cell growth, inducing differentiation and inflammation, which might be relevant in developing epigenetic therapies for human malignancy.

In vertebrates, newly specified HSPCs from the ventral side of dorsal aorta (VDA) migrate into fetal liver (FL) in mammals, or caudal hematopoietic tissue (CHT) in zebrafish, to rapidly expand and differentiate (1–6). Subsequently, HSPCs colonize in the mammalian bone marrow or zebrafish kidney to initiate adult hematopoiesis. The balanced differentiation potential of HSPCs is crucial for maintaining the peripheral blood homeostasis under both physiological and pathological conditions (7). Disrupting this balance may lead to anemia or hematological malignancies (7). Recent single-cell omics analysis in mammals and zebrafish have identified heterogeneous populations of HSPCs with distinct lineage priming and metabolic gene signature (8–10). The continuum of HSPC differentiation is characterized by suppression of cell proliferation-related genes and simultaneous upregulation of lineage-specific regulators, which are orchestrated by extracellular signals within hematopoietic organs (9–11). Epigenetics is a critical process that governs HSPC identity, plasticity, as well as the transition toward new hematopoietic cell states. However, the key epigenetic regulators and mechanisms for coordinating HSPC stemness with balanced differentiation are incompletely understood.

ATF7IP (Activating Transcription Factor 7 Interacting Protein; also known as MBD1-containing chromatin-associated factor (MCAF) or mouse ATFa-associated Modulator (mAM)) is an epigenetic and transcriptional regulator, which recruits transcriptional factors and histone modification enzymes to the general transcription apparatus, thereby modulating chromatin formation and gene expression (12, 13). Transcriptional regulation of ATF7IP facilitates the expression of telomerase reverse transcriptase and other important genes by interacting with ATF7, Specificity protein (SP1) and basal transcription factors TBP/TFIID (12, 14). Evidence of ATF7IP in epigenetic regulation is provided by studies showing that it binds SET domain and bifurcated 1 protein (SETDB1) to mediate transcriptional repression through recruiting MBD (methyl CpG-binding protein) (15, 16). SETDB1 is a lysine methyltransferase (KMT) that catalyzes the trimethylation of histone H3 at lysine 9 (H3K9me3) for silencing genes and endogenous retroviruses (ERVs) in embryonic stem cells (ESCs) or during embryogenesis (17–20). In cultured human cells, ATF7IP regulates SETDB1 nuclear localization and ubiquitination that facilitates the

The authors declare no competing interest.

This article is a PNAS Direct Submission.

[1]J.W., J.L., K.C., and G.L. contributed equally to this work.

[2]To whom correspondence may be addressed. Email: tzhong@bio.ecnu.edu.cn or pengx@seu.edu.cn.

This article contains supporting information online at https://www.pnas.org/lookup/suppl/doi:10.1073/pnas.2209062120/-/DCSupplemental.

Published December 28, 2022.

H3K9 methyltransferase activity (21). Little is known about the impact of Atf7ip in hematopoiesis and the consequence when it is aberrantly expressed. There is little insight into whether and how Atf7ip interacts with Setdb1 or other factors to modulate histone methylation in governing hematopoietic differentiation.

In this study, we report a vertebrate model devoid of Atf7ip or Setdb1, and find that *atf7ip* mutation enhances myeloid differentiation with impaired HSPC expansion and erythropoiesis, concomitant with retrotransposon-triggered inflammation, which phenocopies *setdb1* mutants during embryogenesis. We identify that Atf7ip and Setdb1 regulate HSPC expansion and differentiation by cell-autonomous manners, and reveal the key roles of H3K9me3 deposition and chromatin remodeling mediated by Atf7ip and Setdb1 during HSPC expansion, differentiation, and inflammation. Manipulation of ATF7IP in human HSPCs and myeloid leukemia cells provides mechanistic conservation and pathological consequence. These findings highlight the complex roles and mechanisms of Atf7ip/Setdb1-mediated histone modification in the control of HSPC state and differentiation.

Results

***atf7ip* Mutation Causes a Deficit in T Cells and Erythrocytes.** To understand epigenetics regulation during embryogenesis, a systematic CRISPR/Cas9-mediated genome editing of epigenetics genes on zebrafish chromosomes was conducted (22). Single-guide RNA (sgRNA) was designed to target the third exon of *atf7ip* (Fig. 1*A*). A 7-nucleotide deletion was produced in *atf7ip*$^{-/-}$ mutants (Fig. 1*A*), which was predicted to produce a premature stop codon at amino acid 174 (Fig. 1*B*). The *atf7ip*$^{-/-}$ mutant encoded a truncated peptide lacking the ATF7-interacting protein-binding domain and Fibronectin type III (Fig. 1*B*). Immunoblot analysis indicated a reduction of Atf7ip protein in *atf7ip*$^{-/-}$ embryos (Fig. 1*C*), revealing a loss-of-function mutation. *atf7ip*$^{-/-}$ mutants displayed the reduced blood flow and pericardium edema, leading to embryonic lethality at 6 days post fertilization (dpf) (*SI Appendix*, Fig. S1*A*). Whole-mount in situ hybridization (WISH) analyses showed that *atf7ip* transcripts were maternally deposited in the two-cell-stage embryo, and ubiquitously present throughout the embryo at the eight-somite stage (Fig. 1*D*). From 36 to 40 hpf onward, *atf7ip* was enriched in the brain and the CHT, as well as expressed weekly in the dorsal aorta (Fig. 1*D*). Double fluorescence in situ hybridization (FISH) analysis displayed a significant overlap of *atf7ip* mRNAs with *cmyb* mRNAs in CHT region (Fig. 1*E*). qPCR validated *atf7ip* expression in *CD41*$^{+}$GFP^{+} HSPCs isolated from fluorescence-activated cell sorting (FACS) which increased from 48 to 96 hpf (Fig. 1*F*). Furthermore, the expression of *atf7ip* was far more enriched in *CD41*$^{+}$ HSPCs compared with sorted *flk1*$^{+}$ endothelial cells (ECs) or *elavl3*$^{+}$ neural cells (NCs) in CHT (*SI Appendix*, Fig. S1*B*).

To assess whether *atf7ip*$^{-/-}$ mutation impairs hematopoietic cell differentiation, we analyzed a series of lineage markers in *atf7ip*$^{-/-}$ embryos. WISH showed that expressions of erythroid markers *gata1* and *hemoglobin* (*hbae1*) were markedly reduced in *atf7ip*$^{-/-}$ CHTs compared with wild-type (WT) CHTs at 72 hpf but not earlier stages (32 to 48 hpf) (Fig. 1 *G* and *H* and *SI Appendix*, Fig. S1 *G–J*). Furthermore, the expression of early T cell marker *rag1* or the naïve T cell marker *T cell receptor delta chain* (*tcrd*) was almost absent in the *atf7ip*$^{-/-}$ thymus (Fig. 1*H*). Intriguingly, we found that the expression of myeloid progenitor marker *pu.1* was substantially increased in *atf7ip*$^{-/-}$ mutants, compared with WT siblings at 72 hpf (Fig. 1 *I* and *J*). Moreover, expressions of macrophage marker *mpeg1*, and neutrophil genes *mpx* and *lyz*, were up-regulated in the *atf7ip*$^{-/-}$ CHT (Fig. 1 *I* and *J*) at 72 hpf but not 48 hpf (*SI Appendix*, Fig. S1 *K* and *L*). We further evaluated the total cell number of *gata1*:mCherry or *mpeg1*:EGFP cells in whole embryos by FACS at 72 hpf. Consistent with WISH data, the number of *gata1*$^{+}$mCherry^{+} cells was reduced, whereas the *mpeg1*$^{+}$EGFP^{+} cell number was increased in *atf7ip*$^{-/-}$ embryos (Fig. 1 *K* and *L* and *SI Appendix*, Fig. S1 *C* and *D*).

We next sought to assess whether the primitive hematopoiesis or the development of associated nonhematopoietic tissues was disturbed in Atf7ip-deficient embryos. We found that, the expressions of primitive hematopoietic markers *scl* and *lmo2* at the lateral plate mesoderm, and the expression of erythroid gene *gata1* in the intermediate cell mass, or the myeloid marker *l-plastin* expression in the yolk sac were not perturbed in *atf7ip*$^{-/-}$ mutants compared with WT siblings (*SI Appendix*, Fig. S1 *E* and *F*). Additionally, the development of arterial and venous vasculatures (*flk1*, *deltac*, *dab2*), hedgehog (*vegfaa, shha*) signaling in the midline as well as the formation of somites (*myod*, *nkx3.1*) and pronephros (*cdh17*) showed no apparent changes in *atf7ip*$^{-/-}$ mutants in comparison with WT sibling embryos (*SI Appendix*, Fig. S1 *M–O*), indicating the specific effect of Atf7ip in definitive hematopoiesis.

Loss of Atf7ip Impairs HSPC Expansion and Enhances Myeloid Potential. To evaluate whether *atf7ip* mutation impairs HSPC identity and stemness in developing CHT, we examined HSPC progenitor markers and proliferative cell status in *atf7ip*$^{-/-}$ embryos. WISH showed that the *cmyb* expression was prominently reduced in *atf7ip*$^{-/-}$ CHTs compared with WT controls at 72 hpf, while *cmyb* expression was relatively unaltered in *atf7ip*$^{-/-}$ mutants at 48 hpf (Fig. 2*A* and *SI Appendix*, Fig. S2*B*). Furthermore, a reduction of *runx1*$^{+}$GFP^{+} cells or *cmyb*$^{+}$GFP^{+} cells in the *atf7ip*$^{-/-}$ CHT was detectable at 72 hpf but not 48 hpf (Fig. 2 *B* and *C*). HSPC reduction in CHT was validated by *atf7ip* knockdown using splicing morpholinos; and immunoblot analysis confirmed a reduction of Atf7ip in morphants (*SI Appendix*, Fig. S2 *C–F*). On the contrary, Atf7ip deletion did not perturb HSPC emergence in the VDA, as the expression of *runx1* or *cmyb* failed to reduce in the *atf7ip*$^{-/-}$ VDA at 32 hpf (*SI Appendix*, Fig. S2 *A* and *B*). Furthermore, time-lapse imaging analysis revealed the comparable number of *runx1*$^{+}$*fli1a*$^{+}$ double-positive cells emerging from VDA in *atf7ip*$^{-/-}$/*Tg*(*fli1a*:DsRed/*runx1*:GFP) embryos and control embryos (Fig. 2 *D* and *E*). Collectively, these findings indicate that Atf7ip deficiency causes a reduction of HSPC expansion in developing CHT but not emergence from VDA. We next determined the proliferative status of HSPCs using 5-ethynyl-2-deoxyuridine (EdU) incorporation analysis. *atf7ip*$^{-/-}$/*cmyb*:GFP embryos were pulse labeled using EdU and then coimmunostained for GFP and EdU. Confocal microscopy analysis depicted a marked reduction of *cmyb*$^{+}$EdU^{+} double-positive cells in *atf7ip*$^{-/-}$ embryos compared with WT siblings at 72 hpf but not 48 hpf (Fig. 2 *F* and *G* and *SI Appendix*, Fig. S2*G*). In contrast, TdT mediated dUTP Nick End Labeling (TUNEL) analysis revealed a comparable number of *runx1*$^{+}$TUNEL^{+} positive cells in *atf7ip*$^{-/-}$ mutants and WT siblings at 72 hpf (Fig. 2 *H* and *I*), despite an increase in apoptotic cells over embryos at 72 hpf (*SI Appendix*, Fig. S2*H*). Therefore, loss of Atf7ip reduces the proliferation of HSPCs, and probably accelerates differentiation.

To assess whether the HSPC defects in *atf7ip*-deficient embryos are caused by cell-autonomous effects, we transplanted WT or *atf7ip*-deficient donor cells labeled by rhodamine from *cmyb*:GFP transgenic embryos into nontransgenic WT or *atf7ip*-deficient recipients at the blastula stage. We followed individual recipient embryos at both 36 hpf and 72 hpf. At 36 hpf, a number of HSPCs originating from WT *cmyb*:GFP donors was observed in CHT region in WT and *atf7ip* morphant recipients in 42.1% and 42.3%

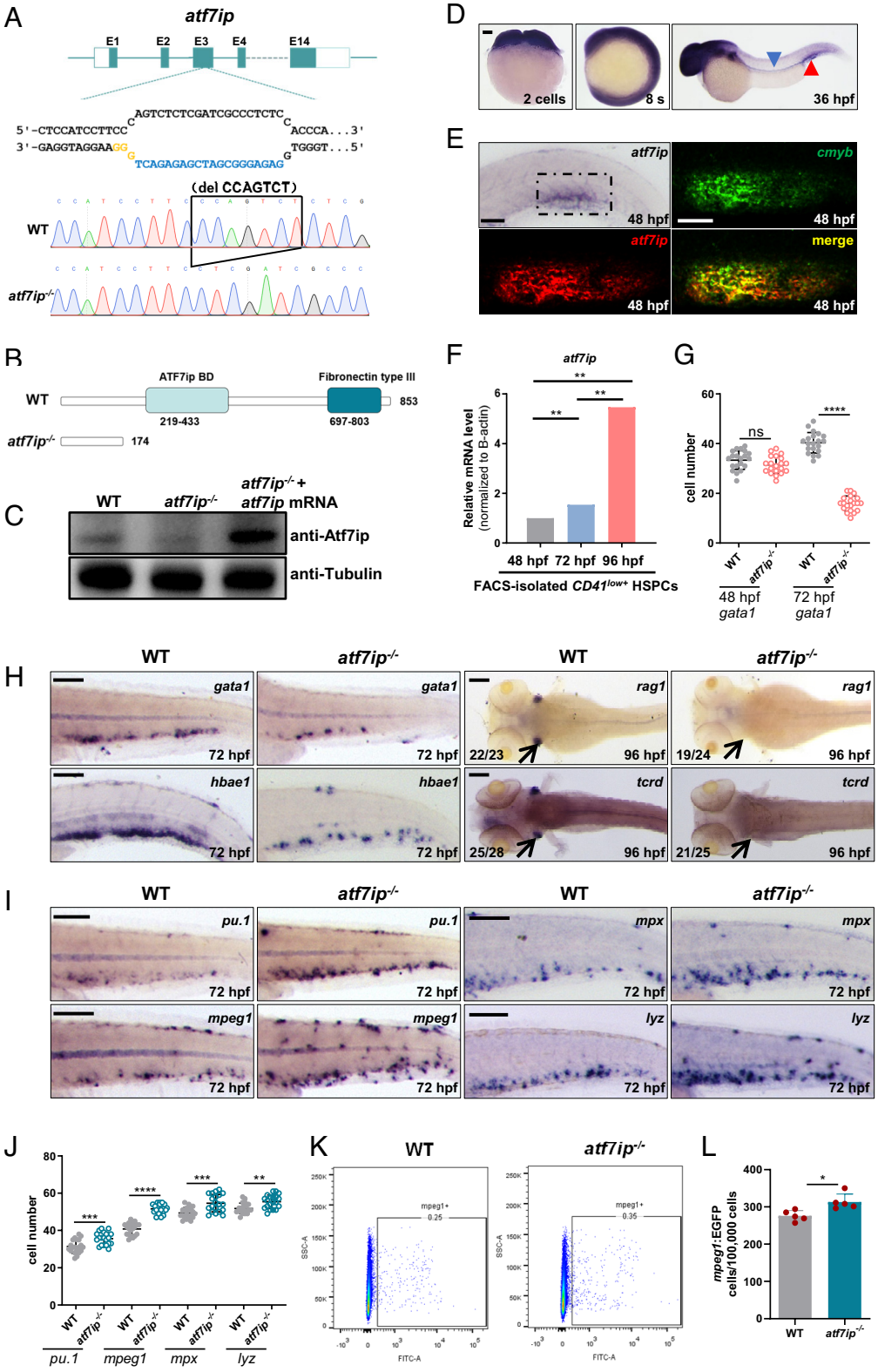

Fig. 1. *atf7ip* mutants exhibit a reduction in T cells and erythroid lineage. (*A*) The sgRNA target sequence of the *atf7ip* allele (blue) and the PAM (yellow) designed in the third exon of *atf7ip* for mutation generation. Electropherograms of *atf7ip* genomic DNA depicting a 7-base deletion. (*B*) The schematic diagram of truncated Atf7ip protein of the homozygous mutant. (*C*) Immunoblotting depicting Atf7ip protein levels in WT siblings, *atf7ip*$^{-/-}$ mutants and *atf7ip* mRNA-injected *atf7ip*$^{-/-}$ mutants at 72 hpf. (*D*) WISH analysis for *atf7ip* expression in WT sibling embryos at various developmental stages. Blue arrow: Dorsal Aorta. Red arrow: CHT region. (*E*) Double FISH revealing the coexpression of green-fluorescence-labeled *atf7ip* with red-fluorescence-labeled *cmyb* in CHT at 48 hpf. Yellow: merged expression of *atf7ip* and *cmyb*. Dashed box: CHT region. (*F*) qPCR analysis showing *atf7ip* expression in *CD41*$^{low+}$ HSPCs at different developmental time. (*G* and *H*) WISH displaying expressions of *gata1* and *hbae1* in CHT, and expressions of *rag1* and *tcrd* in thymus (arrows) in *atf7ip*$^{-/-}$ mutants and siblings at 72 or 96 hpf. Quantification of *gata1*$^{+}$ cells at 48 hpf and 72 hpf is shown in (*G*). (*I* and *J*) WISH analyses of *pu.1, mpeg1, mpx* and *lyz* in WT siblings and *atf7ip*$^{-/-}$ mutants at 72 hpf. Quantification of myeloid cells at 72 hpf is shown in (*J*). (*K* and *L*) Representative FACS analysis of *mpeg1*:EGFP (Enhanced Green Fluorescent Protein) cells in WT embryos and *atf7ip*$^{-/-}$ mutants at 72 hpf. Quantification of *mpeg1*$^{+}$ cells is shown in (*L*). Scale bar, 100 μm (*D*, *E*, *H* and *I*). Quantifications (*F*, *G*, *J*, and *L*) are represented as mean ± SD; *P < 0.05, **P < 0.01, ***P < 0.001, ****P < 0.0001. Student's *t* test.

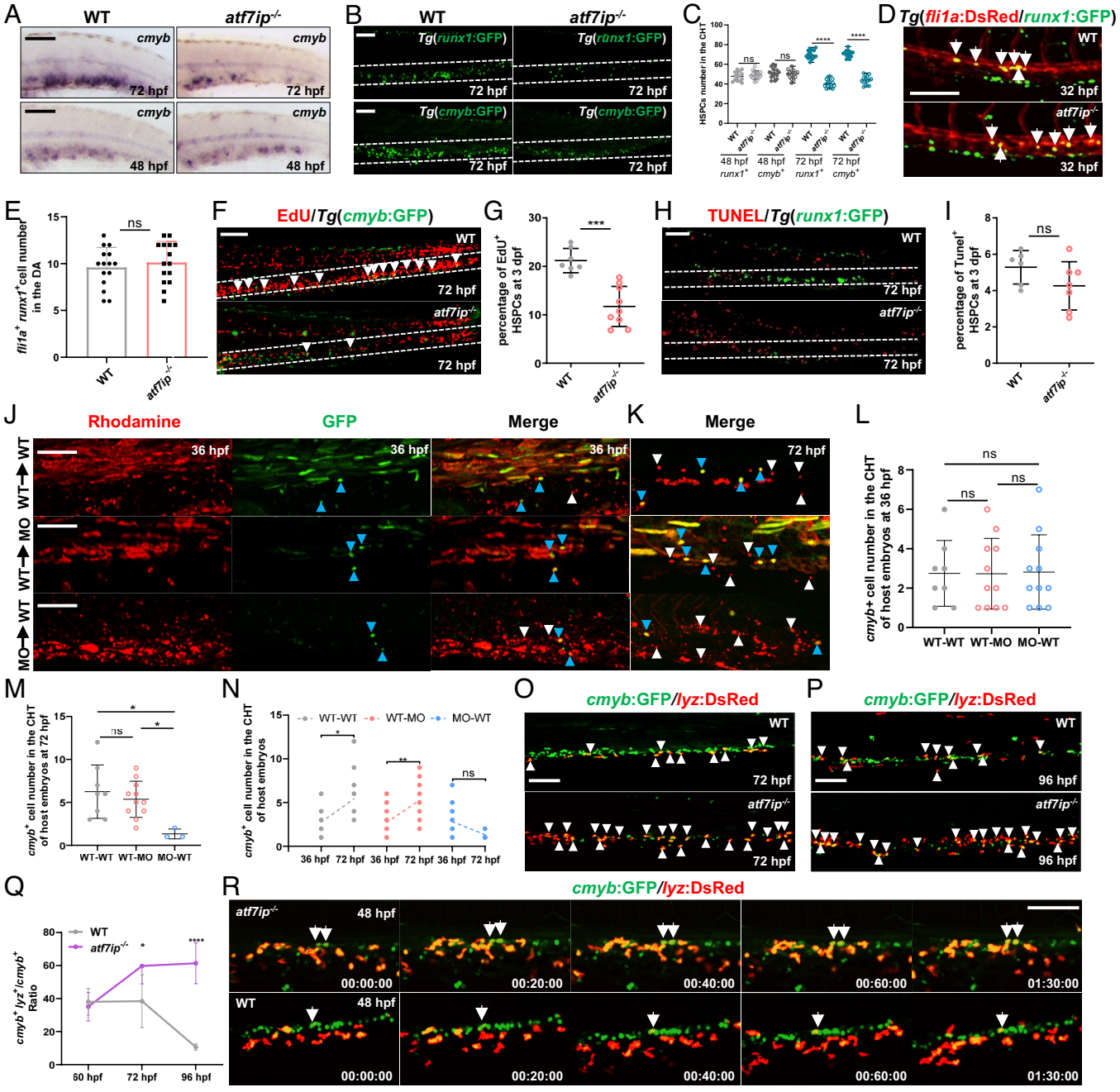

Fig. 2. Atf7ip deficiency decreases HSPC proliferation and enhances myeloid potential. (*A*) WISH depicting expressions of *runx1* and *cmyb* in WT siblings and *atf7ip*$^{-/-}$ mutants at 48 to 72 hpf. (*B*) Confocal imaging showing HSPCs in CHT of *atf7ip*$^{-/-}$ mutants and siblings in *Tg*(*runx1*:GFP) or *Tg*(*cmyb*:GFP) background at 72 hpf. (*C*) Dot chart depicting the quantification of HSPCs number in CHT. (*D* and *E*) Confocal imaging exhibiting emerging HSPCs (arrows) from *fli1a*$^{+}$*runx1*$^{+}$ hemogenic endothelium in VDA in WT siblings and *atf7ip*$^{-/-}$ embryos in *Tg*(*fli1a*:DsRed/*runx1*:GFP) background at 32 hpf. The quantification of *fli1a*$^{+}$*runx1*$^{+}$ precursors number is shown in (*E*). (*F* and *G*) Double immunostaining of *cmyb*$^{+}$EdU^{+} double-positive HSPCs (arrowheads) in WT siblings and *atf7ip*$^{-/-}$ mutants at 72 hpf. Percentages of EdU^{+} HSPCs at 72 hpf are shown in (*G*). (*H* and *I*) Double immunostaining of *runx1*$^{+}$TUNEL^{+} HSPCs in WT controls and *atf7ip*$^{-/-}$ mutants at 72 hpf. Percentages of TUNEL^{+} HSPCs at 72 hpf are shown in (*I*). (*J* and *K*) HSPC reconstitution in CHT of recipient embryos at 36 hpf and 72 hpf. Green fluorescence: *cmyb*$^{+}$GFP cells; Red fluorescence: rhodamine cells. Blue arrowheads: GFP^{+} HSPCs contributed by donor cells; White arrowheads: donor-derived GFP^{-} hematopoietic cells. (*L* and *M*) Quantification of donor-derived *cmyb*$^{+}$ cells in CHT of host embryos at 36 hpf (*L*) and 72 hpf (*M*). (*N*) Linear Regression analysis depicting the variation tendency of the number of donor-derived HSPCs in CHT of host embryos from 36 to 72 hpf. (*O* and *P*) Confocal microscopy revealing *cmyb*$^{+}$*lyz*$^{+}$ double-positive cells (arrowheads) in CHT of *atf7ip*$^{-/-}$ mutants and WT siblings at 72 hpf (*O*) and 96 hpf (*P*). (*Q*) Line chart depicting the rate of HSPCs acquiring myeloid potential in WT embryos and *atf7ip*$^{-/-}$ mutants from 60 hpf to 96 hpf. (*R*) Time-lapse confocal microscopy showing sequential images of HSPCs acquiring myeloid potential (arrows) in *atf7ip*$^{-/-}$ mutants and WT siblings in *cmyb*:GFP/*lyz*:DsRed transgenic background during 1.5 hour-time intervals. Scale bar, 100 μm (*A*, *B*, *D*, *F*, *H*, *J*, *K*, *O*, *P* and *R*). Quantifications (*C*, *E*, *G*, *I*, *L*, *M*, *N* and *Q*) are represented as mean ± SD; *P < 0.05, **P < 0.01, ***P < 0.001, ****P < 0.0001, ns, not significant. Student's *t* test.

transplants, respectively (Fig. 2 *J* and *L* and *SI Appendix*, Fig. S2*I*); and these GFP^{+} HSPC numbers had increased by 72 hpf (Fig. 2 *K*, *M*, and *N*). Reciprocally, *atf7ip*-deficient donor cells transplanted into WT recipient embryos also provided the proximately same number of HSPCs in CHT as WT donor cells in 42.3% transplants at 36 hpf (Fig. 2 *J* and *L* and *SI Appendix*, Fig. S2*I*); however, these GFP^{+} HSPC numbers had not increased, or in some transplants decreased, by 72 hpf (Fig. 2 *K*, *M*, and *N*). These findings suggest that Atf7ip is cell-autonomously required for HSPC survival and expansion in CHT. We next generated parabiotic embryo pairs between *atf7ip*$^{-/-}$ mutants and WT embryos and analyzed the *cmyb*:GFP cell number at 72 hpf. Only a few number

of *cmyb*:GFP HSPCs originated from *atf7ip*$^{-/-}$ mutants were observed in CHT of WT embryos and *atf7ip*$^{-/-}$ mutants, whereas numerous *cmyb*:GFP HSPCs from WT embryos were detectable in CHT of *atf7ip*$^{-/-}$ mutants and WT embryos (*SI Appendix*, Fig. S2 *J–L*), consistent with the transplantation results. To further delineate the HSPC-specific roles of Atf7ip, we generated *tol2* transposon constructs to overexpress WT *atf7ip* fused with mCherry reporter, driven by the *runx1* enhancer, in HSPCs (3, 23). Increased expression of *atf7ip* by the *runx1*/*tol2* system efficiently rescued the declined HSPCs and erythrocytopenia in *atf7ip*$^{-/-}$ mutants, and reversed the expanded myelopoiesis (*SI Appendix*, Fig. S2 *M–O*). By contrast, *atf7ip*-EGFP overexpression in ECs, driven by *fli1a*/*tol2* system, failed to rescue the defects in HSPC expansion and erythropoiesis in *atf7ip*$^{-/-}$ mutants (*SI Appendix*, Fig. S2 *P–R*); neither did *atf7ip*-EGFP expression in ECs reverse the excessive myelopoiesis (*SI Appendix*, Fig. S2 *Q* and *R*). Taken together, these findings demonstrate that the HSPC/hematopoietic cell defects in Atf7ip-deficient embryos are mainly attributed to HSPC intrinsic defects but not influenced by the niche effect.

We reasoned that the expansion of myeloid cells in *atf7ip*$^{-/-}$ mutants originates from the enhanced specification and commitment of myeloid-primed HSPCs that lose proliferative ability. To test the idea, time-lapse imaging analysis was performed to follow the fate change of HSPCs at single-cell resolution in *cmyb*:GFP/*lyz*:DsRed double-transgenic embryos. We observed that the number of *cmyb*$^{+}$*lyz*$^{+}$ double-positive yellow cells (myeloid-primed HSPCs) was markedly increased in *atf7ip*$^{-/-}$ embryos in comparison with WT siblings, while *cmyb*$^{+}$GFP^{+} HSPCs were rarely observed in *atf7ip*$^{-/-}$ mutants (Fig. 2 *O* and *P*). Consistently, the number of *CD41*$^{low+}$*lyz*$^{+}$ double-positive cells was increased in *atf7ip*$^{-/-}$ mutants compared with siblings (*SI Appendix*, Fig. S2 *T–W*). On the contrary, a few *cmyb*$^{+}$*gata1*$^{+}$ double-positive yellow cells (erythroid-biased HSPCs) were detectable (*SI Appendix*, Fig. S2 *X* and *Y*), leading to a reduction of erythroid cells in *atf7ip*$^{-/-}$ embryos. These results suggest that Atf7ip deficiency biased erythroid output to myeloid fate. Notably, time-lapse confocal imaging revealed that, in the *atf7ip*$^{-/-}$ CHT, all of individual *lyz*$^{+}$*cmyb*$^{+}$ cells originated from *cmyb*$^{+}$GFP^{+} cells but not other cell types (Fig. 2*R*). Furthermore, the events for the myeloid commitment (*lyz*$^{+}$*cmyb*$^{+}$) occurred earlier and at a higher rate in *atf7ip*$^{-/-}$ mutants than WT controls over the observation period (Fig. 2 *O–Q* and *SI Appendix*, Fig. S2*S*). These findings demonstrate that Atf7ip restricts HSPCs to differentiation into myeloid-primed HSPCs, leading to distinct lineage differentiation and balanced hematopoiesis.

Atf7ip Interacts with Setdb1 in Regulating Hematopoiesis in CHT. It has been shown that ATF7IP regulates SETDB1 stability and ubiquitination to facilitate its H3K9 methyltransferase activity in cultured cells (16, 21). We postulated that the defective hematopoiesis in Atf7ip-deficient embryos is caused by the reduced Setdb1-mediated H3K9 trimethylation. To test the idea, we examined the Setdb1 protein level in *atf7ip*$^{-/-}$ embryos, and detected a Setdb1 reduction in *atf7ip*$^{-/-}$ embryos (Fig. 3 *A* and *B*). Conversely, *setdb1b* mRNAs in *atf7ip*$^{-/-}$ mutants were unaltered compared with WT siblings (Fig. 3*C*). To substantiate these findings, both *hsp70*:*atf7ip* and *hsp70*:*setdb1b* transgenic zebrafish were generated to induce the expression of *atf7ip* and *setdb1b* by heat shock (Fig. 3*D* and *SI Appendix*, Fig. S3 *A–C*). We observed that the induced *atf7ip* expression restored Setdb1 levels in *atf7ip*$^{-/-}$ embryos, but failed to increase Setdb1 in WT embryos (Fig. 3 *E* and *F* and *SI Appendix*, Fig. S3*D*). We next evaluated the methylation status of H3K9 in the absence of Atf7ip, and found that H3K9me3 was markedly reduced in *atf7ip*$^{-/-}$ embryos compared to WT siblings (Fig. 3 *G* and *H*). Furthermore, induction of Atf7ip or Setdb1 by heat shock in *atf7ip*$^{-/-}$ mutants partially restored the H3K9me3 level (Fig. 3 *G* and *H*). On the contrary, H3K4me3 remained unaltered in *atf7ip*$^{-/-}$ mutants in comparison with WT embryos (*SI Appendix*, Fig. S3*E*). Collectively, these findings demonstrate that the loss of Atf7ip leads to a reduction of H3K9me3 that is dependent on Setdb1. To test whether Atf7ip interacts with Sedb1 in zebrafish, we performed immunoprecipitation experiments in transfected 293T cells with plasmids encoding Flag-tagged zebrafish Atf7ip or HA-tagged zebrafish Setdb1b. Flag-tagged Atf7ip was detectable when HA-tagged Setdb1b was immunoprecipitated. Reciprocally, HA-tagged Setdb1b was detected in the immunoprecipitants of Flag-tagged Atf7ip (Fig. 3 *I* and *J*). Furthermore, double FISH analyses revealed a partial overlap of *setdb1b* mRNAs with *atf7ip* mRNAs in CHT (Fig. 3*K*), in which *setdb1b* mRNAs also overlapped with *cmyb* mRNAs (Fig. 3*L*). Altogether, these findings suggest an interaction between Atf7ip and Setdb1 during embryonic hematopoiesis.

The Setdb1 reduction in *atf7ip*$^{-/-}$ mutants prompted us to test whether *setdb1* overexpression reversed the HSPC-dependent hematopoiesis defects in the absence of Atf7ip. *setdb1b* mRNAs were microinjected into *atf7ip*$^{-/-}$ embryos at the one-to-two-cell stages and performed WISH for *cmyb* (Fig. 3 *M* and *P*). It was evident that *setdb1b* overexpression restored the expression of *cmyb* in the *atf7ip*$^{-/-}$ CHT at 72 hpf, compared with uninjected mutant controls. Likewise, *atf7ip* mRNA injection rescued the *cmyb* reduction in the *atf7ip*$^{-/-}$ CHT. Moreover, coinjections of both *setdb1b* mRNAs and *atf7ip* mRNAs led to a synergistic up-regulation of *cmyb* expression. On the contrary, microinjections of *mbd1b* mRNAs encoding the methyl CpG-binding protein, another Atf7ip interacting factor (13, 15), failed to reverse the *cmyb* reduction in *atf7ip*$^{-/-}$ embryos, suggesting the specific interaction of Atf7ip and Setdb1 during hematopoiesis. To substantiate these findings, *atf7ip*$^{-/-}$/*runx1*:GFP embryos were microinjected with *setdb1b* mRNAs, *atf7ip* mRNAs, or a mixture of *setdb1b and atf7ip* mRNAs (Fig. 3 *N* and *Q*). Either injection of *setdb1b* mRNAs or *atf7ip* mRNAs resulted in an increase of *runx1*$^{+}$GFP^{+} cells in the *atf7ip*$^{-/-}$ CHT, compared with uninjected mutant controls. Furthermore, coinjection of both *setdb1b* mRNAs and *atf7ip* mRNAs caused a marked increase of *runx1*$^{+}$GFP^{+} cells in *atf7ip*$^{-/-}$ embryos. In contrast, the *mbd1b* injection failed to reverse the decline of *runx1*$^{+}$GFP^{+} cells. Next, we evaluated whether Setdb1 induction reversed the myeloid surplus or the erythroid deficit in *atf7ip*$^{-/-}$ mutants using germline-transgenic *hsp70*:*atf7ip* and *hsp70*:*setdb1b* zebrafish. Either induction of *setdb1b* or *atf7ip* by heat shock at 24 hpf, when HSPCs emerge, caused a reduction of *mpx*$^{+}$ cells and increased *hbae1*$^{+}$ cells in the mutant CHT at 96 hpf, in comparison with controls (Fig. 3 *O* and *R* and *SI Appendix*, Fig. S3 *F* and *G*). Moreover, both *setdb1b* and *atf7ip* induction by heat shock resulted in a synergistic reduction of *mpx*$^{+}$ cells but a marked upregulation of *hbae1*$^{+}$ cells in *atf7ip*$^{-/-}$ mutants. Taken together, these findings corroborate the specific interaction of Atf7ip with Setdb1 in mediating definitive hematopoiesis in CHT.

Setdb1 Is Required for HSPC Expansion and Differentiation. To determine the effects of *setdb1* on hematopoiesis during embryogenesis, we generated *setdb1b* mutant by CRISPR/Cas9 in zebrafish. (*SI Appendix*, Fig. S3*H*). Sequencing analysis identified a 5-nucleotide addition in the *setdb1b* mutant (*SI Appendix*, Fig. S3*I*), which predicted a premature stop codon at the amino acid 87 resulting in a truncated peptide (*SI Appendix*, Fig. S3*J*). qPCR and immunoblotting analysis indicated a reduction in *setdb1b* mRNAs and Setdb1 protein, respectively (*SI Appendix*, Fig. S3 *K* and *L*). *setdb1b*$^{-/-}$ embryos displayed the reduced blood flow and pericardium edema, leading to embryonic lethality at 6 dpf

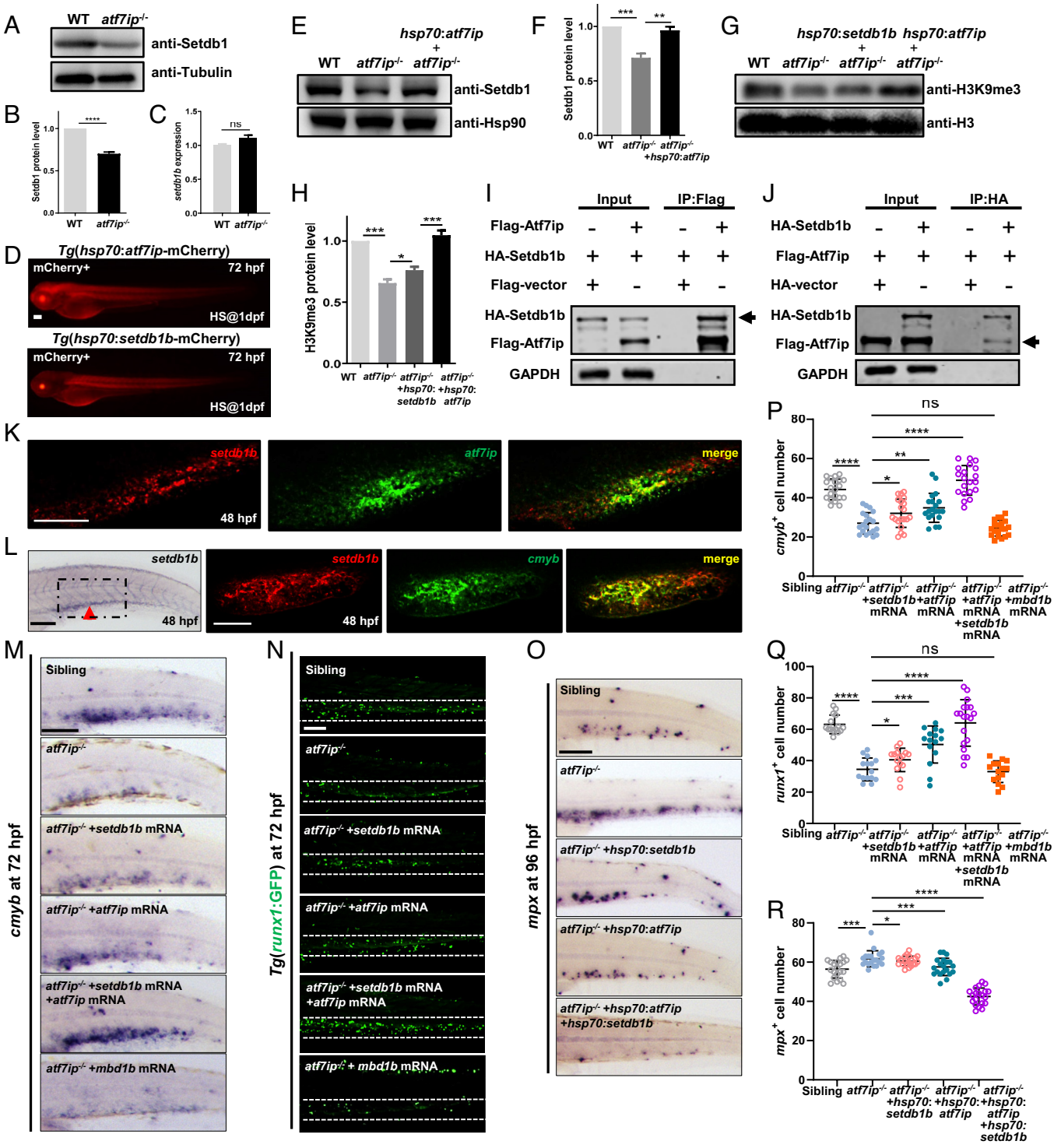

Fig. 3. Interaction of Atf7ip and Setdb1 during hematopoiesis in CHT. (*A* and *B*) Immunoblotting and bar plot showing Setdb1 protein in WT embryos and *atf7ip*$^{-/-}$ mutants at 72 hpf. (*C*) qPCR analysis of *setdb1b* levels in *atf7ip*$^{-/-}$ mutants and siblings at 72 hpf. (*D*) Fluorescent microscopy exhibiting the Atf7ip or Setdb1 induction by heat shock at 72 hpf. (*E* and *F*) Immunoblotting and bar plot depicting Setdb1 levels in WT, *atf7ip*$^{-/-}$ mutants and heat-shocked *atf7ip*$^{-/-}$/*Tg*(*hsp70*:*atf7ip*) embryos at 72 hpf. (*G* and *H*) Western blot and quantification analyses of H3K9me3 levels in WT, *atf7ip*$^{-/-}$ mutants, heat-shocked *atf7ip*$^{-/-}$/*Tg*(*hsp70*:*setdb1b*) embryos and heat-shocked *atf7ip*$^{-/-}$/*Tg*(*hsp70*:*atf7ip*) embryos at 72 hpf. (*I* and *J*) Atf7ip or Setdb1b immunoprecipitation with anti-Flag antibody or anti-HA antibody, respectively. (*K*) Double FISH exhibiting the coexpression of *setdb1b* with *atf7ip* in CHT at 48 hpf. (*L*) Double FISH showing the colocalization of *setdb1b* with *cmyb* in CHT at 48 hpf. Arrow: CHT region. (*M* and *P*) WISH for *cmyb* expression in WT siblings, *atf7ip*$^{-/-}$ mutants, *setdb1b* mRNA-injected *atf7ip*$^{-/-}$ mutants, *atf7ip* mRNA-injected *atf7ip*$^{-/-}$ mutants, *setdb1b*/*atf7ip* mRNA-injected *atf7ip*$^{-/-}$ mutants and *mbd1b* mRNA-injected *atf7ip*$^{-/-}$ mutants at 72 hpf. WISH quantifications are shown in (*P*). (*N* and *Q*) Confocal imaging showing *runx1*$^{+}$ cells in WT siblings, *atf7ip*$^{-/-}$ mutants, *setdb1b* mRNA-injected *atf7ip*$^{-/-}$ mutants, *atf7ip* mRNA-injected *atf7ip*$^{-/-}$ mutants, *setdb1b*/*atf7ip* mRNA-injected *atf7ip*$^{-/-}$ mutants and *mbd1b* mRNA-injected *atf7ip*$^{-/-}$ mutants in *Tg*(*runx1*:*GFP*) background at 72 hpf. Quantification of *runx1*$^{+}$ cells is shown in (*Q*). (*O* and *R*) WISH displaying *mpx* expression in CHT region in siblings, *atf7ip*$^{-/-}$ mutants, heat-shocked *atf7ip*$^{-/-}$/*Tg*(*hsp70*:*setdb1b*) embryos, heat-shocked *atf7ip*$^{-/-}$/*Tg*(*hsp70*:*atf 7ip*), and heat-shocked *atf7ip*$^{-/-}$/*Tg*(*hsp70*:*atf7ip*)/*Tg*(*hsp70*:*setdb1b*) embryos at 96 hpf. WISH quantifications are shown in (*R*). Scale bar, 100 μm (*D*, *K*, *L*, *M*, *N* and *O*). Quantifications (*B*, *C*, *F*, *H*, *P*, *Q*, and *R*) are represented as mean ± SD; *$P < 0.05$, **$P < 0.01$, ***$P < 0.001$, ****$P < 0.0001$, ns, not significant. Student's *t* test.

(*SI Appendix*, Fig. S3*M*). Notably, *setdb1b* expression was detectable in FACS-isolated HSPCs from 48 to 96 hpf (*SI Appendix*, Fig. S3*N*). Furthermore, *setdb1b* expression was more enriched in sorted *CD41*$^{+}$ HSPCs compared with *elavl3* $^{+}$ NCs and *flk1*$^{+}$ ECs in CHT (*SI Appendix*, Fig. S3*O*). Like *atf7ip*$^{-/-}$ mutants, *setdb1b*$^{-/-}$ embryos showed reduced *cmyb* expression in CHT at 96 hpf but not earlier stages (*SI Appendix*, Fig. S3 *R* and *S*). The *cmyb* reduction in CHT was validated by *setdb1b* knockdown using splicing morpholinons (*SI Appendix*, Fig. S3 *X* and *Y*), and the MO efficacy was evaluated by RT-PCR and sequencing (*SI Appendix*, Fig. S3 *V* and *W*). We further detected a decrease of *CD41* $^{+}$ HSPCs in the mutant CHT at 96 hpf (*SI Appendix*, Fig. S3 *T* and *U*). In contrast, the number of *cmyb*$^{+}$ cells or *runx1*$^{+}$ cells emerged from VDA was comparable in *setdb1b*$^{-/-}$ mutants and WT embryos at 32 hpf (*SI Appendix*, Fig. S3 *P*, *Q* and *S*), suggesting that loss of Setdb1 specifically perturbs HSPCs in CHT. We next examined the cell cycle status of *setdb1b*$^{-/-}$ HSPCs by FACS analysis. In *setdb1b*$^{-/-}$ mutants, the HSPC proportion in the G0/G1 phase was increased compared with WT siblings, whereas the HSPC population in the S phase was declined (*SI Appendix*, Fig. S3*Z*). Thus, loss of Setdb1 impairs the entry of HSPCs to the cell cycle, thereby attenuating proliferation, in agreement with the HSPC proliferative defect in *atf7ip*$^{-/-}$ mutants and previous Setdb1 deletion in adult murine HSPCs (24).

To underscore the molecular mechanisms underlying HSPC defects in Setdb1-deficient embryos, we performed RNA-sequencing (RNA-Seq) from embryo trunk-tail regions in *setdb1b*$^{-/-}$ mutants and WT siblings at 96 hpf. RNA profiling analysis identified an increase in expression of 2,192 genes and a reduction in expression of 895 genes in the *setdb1b*$^{-/-}$ transcriptome (*SI Appendix*, Fig. S3*Z1*). Gene set enrichment analysis (GSEA) revealed that categories in "mitotic cell cycle", "DNA replication", were identified in the down-regulated *setdb1b*$^{-/-}$ dataset, whereas biological processes in "immune system process", "inflammatory response", were found in the up-regulated *setdb1b*$^{-/-}$ transcriptome (*SI Appendix*, Fig. S3*Z2*), suggesting the initiation of immune response as a result of loss of Setdb1. As expected, heatmap analysis revealed that *setdb1b*$^{-/-}$ mutants exhibited lower expressions in HSPC stemness and fingerprint genes or erythroid lineage genes, as well as higher expressions in myeloid signature genes or cyclin-dependent kinase inhibitors (CDKNs) (*SI Appendix*, Fig. S3*Z3*). In combination with cell cycle analyses, the transcriptional profiling data illustrate that *setdb1b* mutation impairs HSPC stemness and expansion with enhanced myeloid differentiation and diminished erythropoiesis, accompanied by inflammatory response.

We next validated lineage differentiation defects in *setdb1b*$^{-/-}$ embryos by WISH analysis. It was evident that expressions of erythroid markers *gata1* and *hbae1* or T cell gene *rag1* were decreased in *setdb1b*$^{-/-}$ embryos compared with WT siblings (*SI Appendix*, Fig. S3*Z4*). Conversely, the expressions of myeloid signature genes, including *pu.1*, *lyz*, *mpx*, and *mpeg1* were markedly increased in *setdb1b*$^{-/-}$ mutants (*SI Appendix*, Fig. S3 *Z5* and *Z6*). Furthermore, expressions of *cebpβ* and *granulocyte colony stimulating factor receptor* (*gcsfr*) were up-regulated in *setdb1b*$^{-/-}$ embryos (*SI Appendix*, Fig. S3*Z6*). To assess the HSPC-specific roles of Setdb1 during lineage differentiation, we generated *tol2* transposon constructs to overexpress full-length *setdb1b* fused with *mCherry* reporter, driven by the *runx1* enhancer in HSPCs. Increased expression of *setdb1b* in *runx1*$^{+}$ cells rescued the decreased HSPCs, declined erythropoiesis and biased myeloid differentiation in *setdb1b*$^{-/-}$ mutants (*SI Appendix*, Fig. S3 *Z7*–*Z13*). In contrast, *setdb1b*-EGFP overexpression under the control of *fli1a* promoter/*tol2* transposon system in ECs failed to reverse the decreased HSPCs, and the defects in erythroid and myeloid differentiation (*SI Appendix*, Fig. S3 *Z14*–*Z20*), revealing an HSPC cell-autonomous effect of Setdb1.

Atf7ip Regulates Hematopoiesis through Setdb1-Mediated H3K9me3 Deposition and Chromatin Remodeling. To explore changes and mechanisms in H3K9me3 deposition and chromatin accessibility underlying Atf7ip-mediated hematopoiesis, we performed genome-wide assays for chromatin immunoprecipitation sequencing (ChIP-seq) of H3K9me3 and transposase-accessible chromatin sequencing (ATAC-seq) in *atf7ip*$^{-/-}$ and control HSPCs. *CD41*$^{low+}$ GFP cells were isolated by FACS from *atf7ip*$^{-/-}$ mutants and their siblings at 72 hpf, and subjected to ChIP-seq and ATAC-seq (Fig. 4*A*). Pearson correlation analysis indicated high reproducibility of ChIP-seq data after normalization (Fig. 4*B*). We observed a significant reduction of H3K9me3 marks (42%; 25,612/61,576 total peaks) genome-wide in the absence of Atf7ip (Fig. 4*C*), which is consistent with a global decrease in H3K9me3 protein in whole *atf7ip*$^{-/-}$ embryos (Fig. 3 *G* and *H*). Regions with unaltered and slightly increased H3K9me3 marks were also detectable in the *atf7ip*$^{-/-}$ genome (Fig. 4*C*), suggesting Atf7ip-independent H3K9me3 modifications in those regions. By profiling accessible regions at promoters and intergenic regions, we observed that *atf7ip*$^{-/-}$ and control HSPCs were characterized by specific accessible regions [*atf7ip*$^{-/-}$-open region (10,611 peaks); control-open region (9,693 peaks)], as well as common accessible regions at both *atf7ip*$^{-/-}$ and control HSPCs (Fig. 4*D*). Importantly, decreased H3K9me3 levels correlated with the increased chromatin accessibility in Atf7ip-deficient HSPCs compared with WT HSPCs (Fig. 4*E*), indicating that H3K9me3 deposition facilitates chromatin closure.

We next performed RNA-seq analysis from embryo trunk-tail regions in *atf7ip*$^{-/-}$ mutants and WT siblings. As expected, *atf7ip*$^{-/-}$ mutants up-regulated the expression of myeloid signature genes, and decreased cell cycle genes and erythroid lineage genes (*SI Appendix*, Fig. S4*A*), Gene Ontology also revealed activation of inflammatory response in the absence of Atf7ip, in agreement with *setdb1b*$^{-/-}$ transcriptome analyses (*SI Appendix*, Figs. S3*Z2* and S4*B*). Remarkably, we found that the majority of high-expression genes in *atf7ip*$^{-/-}$ mutants was in regions with increased chromatin accessibility (Fig. 4*F*), which was also associated with reduced H3K9me3 marks (Fig. 4*G*). We then performed overlap analysis between genes increased in the *atf7ip*$^{-/-}$ transcriptome and genes associated with reduced H3K9me3 peaks (Fig. 4*H*). A reduction of H3K9me3 deposition was enriched in zinc-finger genes such as *znf653*, myeloid-related genes *cebpβ, I-plastin, itgam, ddx4* as well as *cyclin-dependent kinase inhibitor 1a* (*cdkn1a/p21*). Notably, a marked reduction of H3K9me3 marks occurred at the promoter and gene body region of *cdkn1a*, the inhibitory G1 checkpoint for HSPC proliferation (25, 26) and the myeloid transcriptional factor *cebpβ* (27, 28). The reduced H3K9me3 regions in *cdkn1a* or *cebpβ* were accompanied by increased chromatin accessibility (Fig. 4*I*), revealing *cdkn1a* and *cebpβ* as targets of Atf7ip-mediated H3K9 trimethylation. We validated the increased expression of *cdkn1a* and *cebpβ* by RT-qPCR in *atf7ip*$^{-/-}$ HSPCs (*SI Appendix*, Fig. S4 *C* and *D*).

To assess the cooperation of Atf7ip and Setdb1 in mediating H3K9 trimethylation, we conducted ChIP-PCR in *atf7ip*$^{-/-}$/*hsp70*:-*setdb1b* embryos using H3K9me3 antibody. Setdb1b induction by heat shock in *atf7ip*$^{-/-}$ embryos increased the enrichment of H3K9me3 in the *cdkn1a* or *cebpβ* promoter (Fig. 4*J*), in agreement with the increased H3K9me3 protein by Setdb1 induction in whole *atf7ip*$^{-/-}$ embryos (Fig. 3 *G* and *H*). As a result, the upregulation of *cdkn1a* or *cebpβ* was repressed in heat-shocked *atf7ip*$^{-/-}$/*hsp70*:-*setdb1b* embryos (Fig. 4*K*). Next, we performed Setdb1 ChIP-seq and H3K9me3 ChIP from sorted HSPCs (*SI Appendix*, Fig. S5

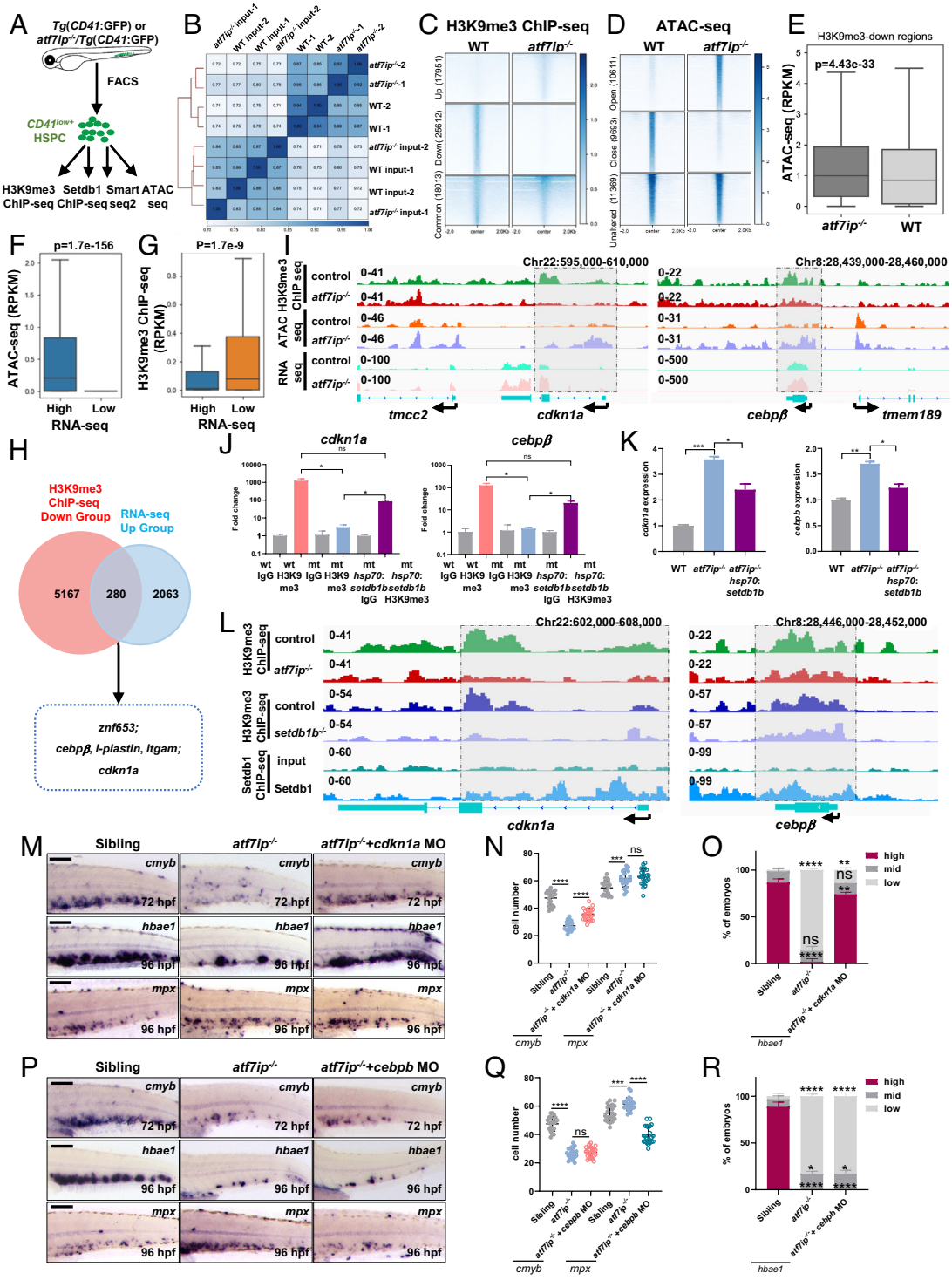

Fig. 4. Atf7ip cooperates with Setdb1 to mediate H3K9me3 deposition and chromatin remodeling. (*A*) Schematic workflow of H3K9me3 ChIP-seq, Setdb1 ChIP-seq, Smart-seq2 and ATAC-seq from FACS-sorted *CD41*:GFP HSPCs in siblings and *atf7ip*$^{-/-}$ mutants at 72 hpf. (*B*) Heat maps showing the correlation between biological replicates of H3K9me3 ChIP-seq samples generated in *atf7ip*$^{-/-}$ and WT HSPCs at 72 hpf. (*C*) Heat maps for differentially and commonly enriched H3K9me3 peaks identified in whole genome in WT and *atf7ip*$^{-/-}$ HSPCs. Peaks: mutant-specific group (*Top*), control-specific group (*Middle*), and common group (*Bottom*). (*D*) Heat maps for differentially and commonly enriched ATAC-seq peaks identified in the whole genome in WT and *atf7ip*$^{-/-}$ HSPCs. Peaks: open (*Top*), close (*Middle*), and unaltered (*Bottom*). (*E*) Box plot showing chromatin accessibility levels in reduced H3K9me3 regions in *atf7ip*$^{-/-}$ and WT HSPCs. Y-axis: RPKM of ATAC-seq data. *P* value by Mann–Whitney *U* test. (*F*) The box plot exhibiting the correlation between chromatin accessibility levels and gene expression levels at promoter regions in *atf7ip*$^{-/-}$ mutants. (*G*) The box plot showing the inverse correlation between H3K9me3 and gene expression levels at gene regions in *atf7ip*$^{-/-}$ mutants. (*H*) Venn diagram displaying overlaps between gene-sets with reduced H3K9me3 levels and gene-sets with increased RNA-seq levels in *atf7ip*$^{-/-}$ mutants. (*I*) Integrative Genomics Viewer (IGV) tracks exhibiting marks of H3K9me3-ChIP, ATAC-seq and RNA-seq at the locus of *cdkn1a* or *cebpβ* in WT and *atf7ip*$^{-/-}$ mutants. (*J*) ChIP-qPCR analysis of H3K9me3 levels in the promoter of *cdkn1a* or *cebpβ* in WT, *atf7ip*$^{-/-}$ mutants and heat-shocked *atf7ip*$^{-/-}$/*Tg*(*hsp70*:*setdb1b*) HSPCs. (*K*) qPCR analyses of *cdkn1a* or *cebpβ* expression in WT, *atf7ip*$^{-/-}$ mutants and heat-shocked *atf7ip*$^{-/-}$/*Tg*(*hsp70*:*setdb1b*) embryos at 72 hpf. (*L*) IGV displaying H3K9me3-ChIP and Setdb1-ChIP marks at the locus of *cdkn1a* or *cebpβ* in controls, *atf7ip*$^{-/-}$ and *setdb1b*$^{-/-}$ HSPCs. (*M*–*O*) WISH showing expressions of *cmyb*, *hbae1* or *mpx* in WT siblings, *atf7ip*$^{-/-}$ embryos, and *cdkn1a* MO-injected *atf7ip*$^{-/-}$ embryos. WISH quantifications are shown in (*N*) and (*O*). (*P*–*R*) WISH displaying expressions of *cmyb,hbae1* or *mpx* in WT siblings, *atf7ip*$^{-/-}$ embryos, and *atf7ip*$^{-/-}$ embryos with *cebpβ* MO-injection. WISH quantifications are shown in (*Q*) and (*R*). MO, antisense morpholinos. (Scale bar, 100 μm.) (*M* and *P*). *P* values by Mann–Whitney *U* tests (*F* and *G*): *P* = 1.7e−156 (*F*), *P* = 1.7e−9 (*G*). The center of the box plots represents the median value. Student's *t* test was conducted (*J*, *K*, *N*, *O*, *Q*, and *R*): mean ± SD. *$P < 0.05$, **$P < 0.01$, ***$P < 0.001$, ****$P < 0.0001$, ns, not significant. Student's *t* test.

A–D). It was evident that Setdb1-ChIP marks mostly distribute to 5-UTR, promoter and gene body regions, in addition to transposon and intergenic regions (*SI Appendix*, Fig. S5*E*). About 38% increased or 26% decreased genes in *setdb1b*$^{-/-}$ transcriptome were bound by Setdb1 (*SI Appendix*, Fig. S5*F*), suggesting that Setdb1 regulates gene transcription mainly by repressing Setdb1-bound target genes (29). Integrated analyses between genes bound by Setdb1 and genes up-regulated in both *setdb1b*$^{-/-}$ and *atf7ip*$^{-/-}$ transcriptomes identified 75 genes, including *cdkn1a* and *cebpβ* (*SI Appendix*, Fig. S5*G*). The Setdb1-ChIP marks were detectable at the locus of *cdkn1a* or *cebpβ* (Fig. 4*L*), revealing the direct binding of these genes by Setdb1. Analyses of *atf7ip*$^{-/-}$ and *setdb1b*$^{-/-}$ H3K9me3 ChIP-seq datasets displayed an overlap in reduced H3K9me3-ChIP marks between *atf7ip*$^{-/-}$ and *setdb1b*$^{-/-}$ mutants (*SI Appendix*, Fig. S5*H*), suggesting that Atf7ip and Setdb1 share part of their histone methylation targets (29). Notably, *setdb1b*$^{-/-}$ HSPCs exhibited a reduction of H3K9me3 marks in the same promoter/gene body region of *cdkn1a* or *cebpβ* as *atf7ip*$^{-/-}$ HSPCs (Fig. 4*L*). We next tested whether depletion of *cdkn1a* or *cebpβ* reversed hematopoiesis defects in Atf7ip- or Setdb1-deficient embryos. *cdkn1a* knock down by antisense-morpholinos injection rescued the loss of HSPC expansion and erythrocytopenia in *atf7ip*$^{-/-}$ or *setdb1b*$^{-/-}$ embryos, but failed to reverse the expanded myelopoiesis (Fig.4 *M–O* and *SI Appendix*, Fig. S4 *E–K*), suggesting that erythrocytopenia derives from the defective HSPC expansion. Furthermore, microinjection of *cebpβ* morpholinos suppressed the enhanced myelopoiesis but failed to rescue the decline of HSPCs and erythrocytes in *atf7ip*$^{-/-}$ or *setdb1b*$^{-/-}$ mutants (Fig. 4 *P–R* and *SI Appendix*, Fig. S4 *L–N*), revealing the specific effect of *cebpβ* in driving myeloid differentiation. By contrast, HSPC emergency in the AGM region of *atf7ip*$^{-/-}$ and *setdb1b*$^{-/-}$ mutants was unaffected by *cdkn1a* or *cebpβ* knockdown (*SI Appendix*, Fig. S4 *O–T*).

H3K9me3 Reduction in HSPCs Derepresses Repetitive Elements that Activate Rig-l/Mad5-Mediated Inflammatory Signaling. We found that H3K9me3 marks in HSPCs mostly distribute to zebrafish DNA transposons (DNAs), and retrotransposons including long terminal repeats (LTRs) and long interspersed nuclear elements (LINEs), in addition to depositions in gene bodies and regulatory regions (Fig. 5*A*). Therefore, we assessed whether loss of Atf7ip or Setdb1 caused derepression of DNA transposons or retrotransposons through reduced H3K9me3 marks. We found that *atf7ip*$^{-/-}$ or *setdb1b*$^{-/-}$ HSPCs exhibited an overall reduction of H3K9me3 depositions in DNAs, LTRs and LINEs (Fig. 5*B* and *SI Appendix*, Fig. S5*I*), which correlated with increased open chromatin (Fig. 5*C* and *SI Appendix*, Fig. S5*J*), resulting in upregulation of LTR and LINE retroelements (Fig. 5*D* and *SI Appendix*, Fig. S5*K*). However, the increased or decreased expression of DNA transposon numbers were comparable (Fig. 5*D* and *SI Appendix*, Fig. S5*K*). Notably, the reduced H3K9me3 marks and increased retroelement expression were present in a subset of LTR/LINE retrotransposons, including Gypsy II, Ngaro or L2 superfamily in Atf7ip- or Setdb1-deficient HSPCs (Fig. 5*E* and *SI Appendix*, Fig. S5 *L* and *M*). Examples of Copia-8 and L2-1 retroelement were visualized by Integrative Genomics Viewer (IGV) browser (Fig. 5*F*), highlighting H3K9me3-mediated chromatin organization in specific retrotransposon expression in HSPCs.

It has been shown that active repetitive elements such as retrotransposon can activate cytoplasmic RNA sensor-mediated inflammatory pathways during embryogenesis, HSPC formation and tumor immunotherapy (30–33). In *atf7ip*$^{-/-}$ and *setdb1b*$^{-/-}$ mutants, we identified that type-I Interferon (IFN) response mediated by Mda5/Rig-l-like receptor (RLR) pathway was strongly up-regulated, including Rig-l/Mda5 receptors, interferon regulatory factors (*irf3*/*irf7*), NF-κB subunits (*nfκb1/nfκb2*), type I IFN (*ifnphi1/ifnphi3*), and NF-κB/IFN target genes (*il1β, isg20, gcsf, cxcl18b*) (Fig. 5*G*), most of which have been validated by Smart-seq analyses from sorted HSPCs (*SI Appendix*, Fig. S6*A*). Notably, retrotransposons derived from *GypsyII*, *Ngaro* and *L2* superfamilies start to derepress at 48 hpf by loss of Atf7ip or Setdb1 (*SI Appendix*, Fig. S6 *G* and *H*); and the full activation and upregulation of Mda5/RLR-mediated inflammation genes proceed at 72 hpf (*SI Appendix*, Fig. S6 *G* and *H*). These results suggest that the RLR-mediated inflammatory response triggered by derepression of Atf7ip/Setdb1-dependent TEs proceeds at the embryonic stage, when HSPCs undergo hematopoietic differentiation. Motif analysis identified the enrichment of key transcription-factor binding sites Zscan4, Irf, Stat in gained accessibility regions in Atf7ip-deficient HSPCs (Fig. 5*H*). Zscan4 activates LTR/endogenous retrovirus (ERV) expression (34); IRF and STAT can promote immune and myeloid genes such as *ISGs* and *CEBPβ* transcription (35, 36). These findings are consistent with the preferential expression of retrotransposons, inflammation, and myeloid genes upon loss of Atf7ip or Setdb1. Notably, depletion of Rig-I or Mda5 in *atf7ip*$^{-/-}$ or *setdb1b*$^{-/-}$ mutants reduced the upregulation of type-I IFN (*ifnphi1*) and its downstream genes (*il1β*, *irf9*, *isg20*, *stat1a*, *gcsf*), including myeloid factor (*cebpβ*) and derivative genes (*mpeg1* and *mpx*) (Fig. 5 *I* and *J*). The excessive myelopoiesis in *atf7ip*$^{-/-}$ or *setdb1b*$^{-/-}$ mutants was also partially reversed (Fig. 5 *K* and *L*). However, knockdown of *rig-I* receptor failed to rescue the declined HSPCs and erythrocytopenia in *atf7ip*$^{-/-}$ mutants (*SI Appendix*, Fig. S6 *B–E*), suggesting that the HSPC and erythroid deficits are independent of the RLR-mediated inflammatory pathway. Notably, treatment of the reverse transcriptase inhibitor Foscarnet suppressed the activation of type-I IFN signaling and myeloid gene expression, revealing that the reverse-transcribed cDNAs from retroviral RNAs may also trigger inflammation upon Atf7ip loss (*SI Appendix*, Fig. S6*F*). Furthermore, temporal treatment of BX795, a Mda5/RLR signaling inhibitor or Foscarnet from 48 to 72 hpf, suppressed the upregulation of inflammatory response genes and excessive myelopoiesis in *atf7ip*$^{-/-}$ and *setdb1b*$^{-/-}$ mutants (*SI Appendix*, Fig. S6 *I–N*), corroborating the activation of RLR-mediated inflammatory response at this temporal stage by loss of Atf7ip or Setdb1. Altogether, these findings illustrate that Atf7ip/Setdb1-mediated H3K9me3 deposition silences transposable elements to prevent biased myelopoiesis by repressing interferon response, which is mediated in part through viral RNA-sensor signaling pathways.

Roles of ATF7IP in Human Normal and Malignant Hematopoiesis. To investigate whether ATF7IP plays a conserved role in mammals, we analyzed the ATF7IP expression pattern by analyzing single-cell RNA-seq data in the human fetal liver (37). ATF7IP was enriched in HSPCs, and detectable in CMPs, GMPs and MEPs (Fig. 5*M*). We next mutated ATF7IP in human CD34^{+} HSPCs using CRISPR/Cas9 edition technology (38). sgRNAs targeting the ATF7IP exon 2 and ribonucleoprotein (RNP) complex were electroporated into human CD34^{+} cells (Fig. 5*N*). DNA sequencing analysis revealed 85 to 99% editing frequency (*SI Appendix*, Fig. S7*A*), suggesting ATF7IP deficiency. We then performed in vitro colony assays, and found that colony forming units of granulocyte, erythrocyte, monocyte, and megakaryocyte (CFU-GEMM) or erythrocyte (CFU-E) were profoundly reduced upon ATF7IP depletion. However, the granulocyte-macrophage colony forming ability (CFU-GM) was comparable in *ATF7IP*$^{-/-}$ CD34^{+} HSPCs and control HSPCs (*SI Appendix*, Fig. S7*B*). Consequently, the proportion of CFU-GEMM or CFU-E was reduced, while the proportion of CFU-GM was increased (*SI Appendix*, Fig. S7*C*). Furthermore, the number of large colony (> 3.5 mm) formed by ATF7IP-deficient CD34^{+} HSPCs was markedly declined compared with control CD34^{+} HSPCs (*SI*

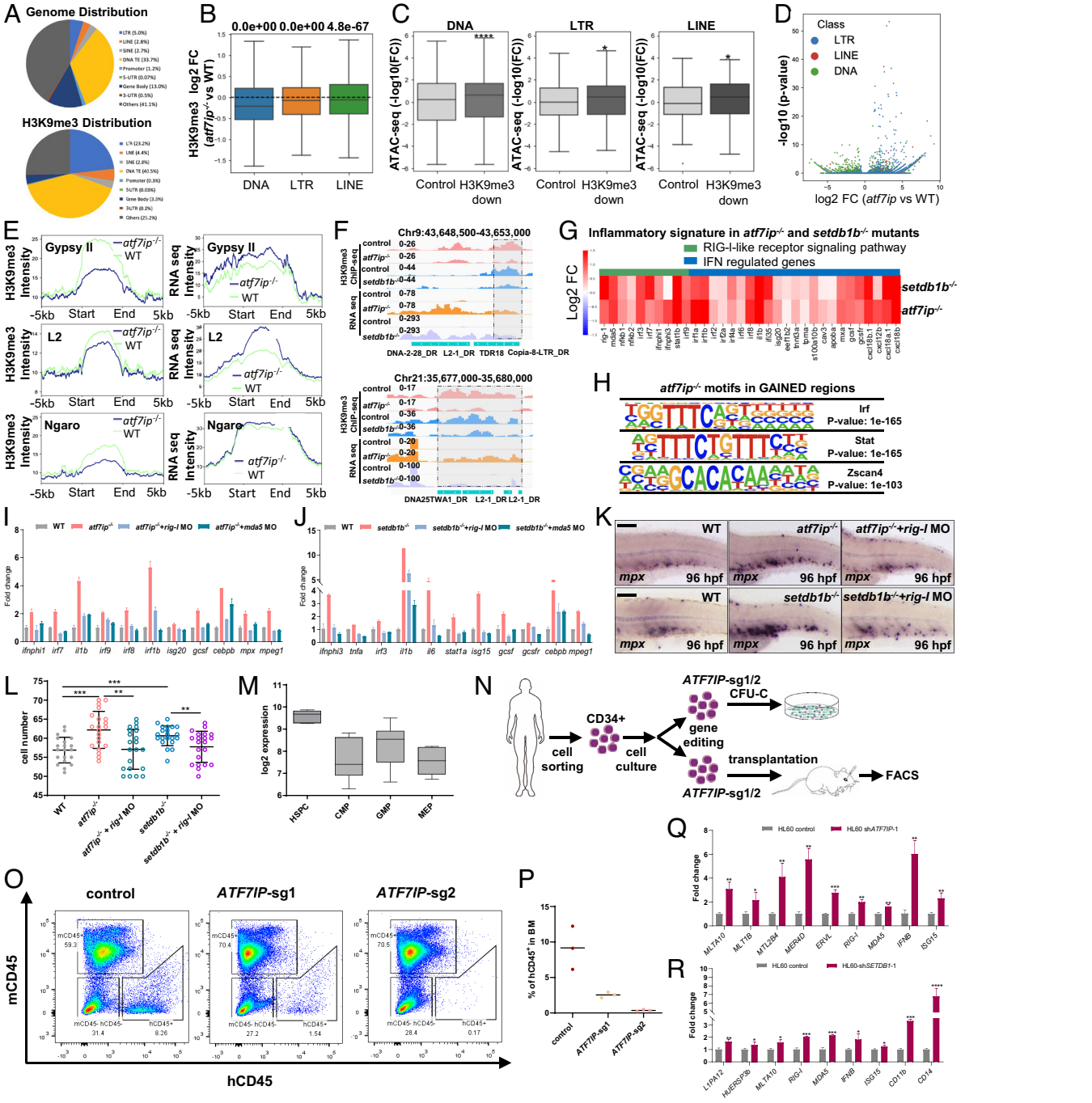

Fig. 5. Roles of Atf7ip/Setdb1 in RLR-mediated inflammatory response and human hematopoiesis. (*A*) Pie charts exhibiting distributions of genes and transposable elements (*Up*) and distributions of H3K9me3 marks (*Down*) in the zebrafish genome. (*B*) Box plots showing distributions of Log2 fold changes of H3K9me3 at DNA TEs, LTRs or LINEs between WT controls and *atf7ip*$^{-/-}$ HSPCs. *P* values by one-sample *t* tests. (*C*) Box plots of chromatin accessibility levels in H3K9me3-depleted (H3K9me3 fold change <30 percentile) and control (H3K9me3 fold change >70 percentile) TE regions. Mann–Whitney *U* test was performed between H3K9me3-delpeted and control TE regions, *P* = 8.44e−05 (DNA TE), *P* = 1.49e−02 (LTR), *P* = 4.37e−02 (LINE). (*D*) Volcano plot for differential expression analysis of DNA TEs, LTRs and LINEs in WT and *atf7ip*$^{-/-}$ mutants. X-axis: $\log_2$-transformed fold changes of TE levels between *atf7ip*$^{-/-}$ mutants and controls. Y-axis: $-\log_{10}$-transformed adjusted *P*-values calculated by DEseq2. Among differentially regulated (adjusted *P*-value < 0.05) TEs, 69.9% (n = 2,510) of DNA TEs, 95.2% (n = 2,358) of LTRs and 90.8% (n = 687) of LINEs are up-regulated. (*E*) Metagene profiles of H3K9me3 and RNA-seq normalized signal intensities for Gypsy II, Ngaro, and L2 TE super families in WT and *atf7ip*$^{-/-}$ HSPCs. Regions are aligned by transcription start sites (TSS) and transcription end sites (TES) of TEs. Profiles represent median intensity levels of each group. (*F*) IGV tracks showing reduced H3K9me3 signals and increased expression at retrotransposon locus in siblings, *atf7ip*$^{-/-}$and *setdb1b*$^{-/-}$ HSPCs. (*G*) Heatmap depicting fold changes of common inflammatory signature genes in *atf7ip*$^{-/-}$ or *setdb1b*$^{-/-}$ mutants versus respective controls (cutoff fold change 1.5, *P* < 0.05). (*H*) Motif sequences enriched in gained ATAC-seq peaks in *atf7ip*$^{-/-}$ mutants. (*I*) qPCR analyses of RLR targets, common inflammatory genes, and myeloid genes in WT, *atf7ip*$^{-/-}$ mutants, *rig-I* MO or *mda5* MO-injected *atf7ip*$^{-/-}$ mutants. (*J*) RT-qPCR analyses of RLR targets, common inflammatory gene and myeloid gene expression in WT, *setdb1b*$^{-/-}$ mutants, *rig-I* MO or *mda5* MO-injected *setdb1b*$^{-/-}$ mutants. (*K* and *L*) WISH analyses of *mpx* in respective controls, *atf7ip*$^{-/-}$ mutants, *rig-I* MO-injected *atf7ip*$^{-/-}$ mutants; and *setdb1b*$^{-/-}$ mutants, *rig-I* MO-injected *setdb1b*$^{-/-}$ mutants at 96 hpf. WISH quantifications are shown in (*L*). (*M*) Box plot exhibiting ATF7IP expression patterns in human fetal liver. (*N*) Schematic illustrations of CFU-C assay and transplantation experiment using human *ATF7IP*-deficient CD34^{+} HSPCs. (*O*) FACS analysis showing percentages of human CD45^{+} and mouse CD45^{+} cells in mouse bone marrow 2 months after transplantation. (*P*) Dot chart exhibiting human cell chimerism [%hCD45^{+}/(%hCD45^{+} + %mCD45^{+})] in mouse bone marrow after transplantation. (*Q*) RT-qPCR analyses of ERVs, RLR-mediated inflammatory genes in HL60 cells with control or *ATF7IP* shRNA. (*R*) RT-qPCR analyses of ERVs, *CD11b*, *CD14*, and RLR-mediated inflammatory genes in HL60 cells with control or *SETDB1* shRNA. Scale bar, 100 μm (*K*). Quantifications (*I*, *J*, *L*, *M*, *P*, *Q*, and *R*) are represented as mean ± SD; *P < 0.05, **P < 0.01, ***P < 0.001, ****P < 0.0001, ns, not significant. Student's *t* test.

Appendix, Fig. S7*D*), indicating the decreased HSPC expansion and preserved myeloid potential upon loss of ATF7IP. To assess the role of human ATF7IP during hematopoiesis in vivo, we transplanted *ATF7IP*$^{-/-}$ CD34^{+} HSPCs into immunodeficient NCG-X mice containing c-kit mutation (39). ATF7IP depletion significantly reduced the chimerism of human CD45^{+} HSPCs in comparison to transplanted control CD34^{+} HSPCs (Fig. 5 *O* and *P*), indicating the impaired HSPC stemness and self-renewal in the absence of ATF7IP. Furthermore, ATF7IP-deficient CD34^{+} HSPCs showed an increased percentage of CD33^{+} myeloid cells in transplanted mice (*SI Appendix*, Fig. S7 *E* and *F*). These findings, together with the results obtained in zebrafish, corroborated ATF7IP as a conserved regulator for HSPC expansion and differentiation.

Considering that ATF7IP restricts myeloid potential and maintains the HSPC proliferative state, we next assessed whether aberrant ATF7IP expression correlates with human leukemia. By analyzing acute myeloid leukemia (AML) TCGA dataset (http://bloodspot.eu), ATF7IP was identified to be highly expressed in human AML cells (*SI Appendix*, Fig. S7*H*). We therefore knocked down ATF7IP using a short-hairpin approach in leukemic HL60 cells (*SI Appendix*, Fig. S7*G*). Cell Counting Kit-8 (CCK8) assays indicated that proliferation of HL60 cells was attenuated by ATF7IP depletion (*SI Appendix*, Fig. S7*I*). Furthermore, we observed the increased expression of *CDKN1A*, *CEBPβ*, and myeloid markers *CD11b*, *CD14* (*SI Appendix*, Fig. S7 *K–N*), suggestive of cell growth repression via myeloid differentiation. Notably, LTR/ERVs such as *MLTA10, MLT1B, MER4D* and the RLR-mediated inflammation genes including *RIG-I*, *MDA5*, *IFN, ISG15* were substantially up-regulated (Fig. 5*Q*). These cellular and molecular alterations were recapitulated in ATF7IP-depleted leukemic OCI-AML cells (*SI Appendix*, Fig. S7 *J* and *O*). Similarly, SETDB1 depletion in HL60 cells inhibited cell proliferation and induced myeloid differentiation, concomitant with retrotransposon-triggered inflammation (Fig. 5*R* and *SI Appendix*, Fig. S7 *P–S*) (40). Collectively, these findings demonstrate that depletion of ATF7IP or SETDB1 in human myeloid leukemia cells up-regulates CDKN1A/P21 and CEBPβ and induces TE-triggered inflammation, thereby suppressing leukemic cell growth and inducing myeloid differentiation, consistent with their regulation during hematopoiesis.

Discussion

In this study, we have demonstrated that the epigenetic regulator Atf7ip plays a conserved role in coordinating HSPC expansion with hematopoietic differentiation in zebrafish and human. The interaction of Atf7ip and Setdb1 is important for controlling definitive hematopoiesis in CHT. Mechanistically, Atf7ip regulates hematopoiesis through Setdb1-mediated H3K9me3 deposition and chromatin remodeling (*SI Appendix*, Fig. S8). Loss of Atf7ip or Setdb1 causes a reduction of H3K9me3 marks in hematopoietic master regulators such as *cdkn1a* and *cebpβ*, accompanied by increased chromatin accessibility, leading to enhanced myeloid differentiation with impaired HSPC expansion and erythropoiesis. Concomitantly, Atf7ip and Setdb1 are required for silencing a subset of retrotransposons (Gypsy II, Ngaro or L2 superfamily) through H3K9me3 depositions to prevent RLR-mediated inflammation and myelopoiesis. Manipulations of human HSPCs and myeloid leukemia cells corroborate ATF7IP/SETDB1 as conserved cell-autonomous regulators for HSPC expansion and differentiation. These findings provide insight into Atf7ip/Setdb1-mediated H3K9me3 deposition and chromatin remodeling in the control of HSPC stemness state and hematopoietic differentiation.

Our time-lapse imaging analysis revealed that the expansion of myeloid cells upon Atf7ip deletion derives from the increased myeloid-primed HSPCs that lose proliferative ability. Similarly, *setdb1b*$^{-/-}$ mutants exhibited the reduced HSPC proliferation and enhanced myeloid differentiation. In humans, ATF7IP depletion in CD34^{+} HSPCs impairs HSPC expansion and repopulation with preserved myeloid differentiation and declined erythropoiesis. These findings highlight Atf7ip as the epigenetic gatekeeper of myeloid potential that governs HSPC identity, expansion, and the transition toward differentiated cells. We have mapped genome-wide changes of H3K9me3 distribution and chromatin accessibility and revealed that changes of chromatin configuration were associated with differential H3K9me3 levels. Previous studies reported that the reduced H3K9me3 levels by Setdb1 deletion results in a derepression of genes and TEs at transcriptomic levels (17, 18). However, it is unclear whether such changes take place through chromatin alterations caused by loss of H3K9me3. Depletion of histone H3.3, the substrate of H3K9me3, causes opening of heterochromatin in murine ESCs (41). Histone H3.3 can modulate chromatin adaptability via the interplay between H3K9me3 and H3K27me3 depositions (36). Our findings support the specific effect of H3K9me3 modification in adjusting chromatin configuration for regulating genes and transposable elements during hematopoiesis. The polycomb group for H3K27me3 modification plays a principal role in regulating HSPC self-renewal and differentiation (42, 43). It is of high importance to test the collaboration between the Atf7ip/Sedb1 complex and polycomb group during hematopoietic development and homeostasis.

Recent studies have shown the association between histone/DNA hypomethylation in TEs and induction of viral sensor-mediated inflammation during embryogenesis, HSPC formation or tumor immunotherapy (30, 32, 33). Our studies provide evidence that links the loss of Atf7ip/Setdb1-mediated H3K9me3 deposition with TE-triggered RLR inflammatory response during hematopoietic differentiation. This is distinct from the early RLR-mediated inflammation pathway in controlling HSPC generation from AGM, which might be triggered by other TE derepression mechanisms in ECs (33). Previous studies reported that Setdb1 deletion in CD34^{+} LSKs or GMPs in adult murine bone marrow resulted in a mild reduction of H3K9me3 in TEs and limited increases of LTR/ERVs as well as derepression of gluconeogenic enzymes (24). These differences may reflect distinct H3K9me3 targeting mechanisms mediated by Setdb1 during hematopoietic development and homeostasis. Our findings are consistent with the roles of Setdb1-controlled H3K9me3 modification in silencing LTR/ERVs in mouse ESCs and tumor cells (17, 30, 44). Notably, we find a significant reduction of H3K9me3 deposition in hematopoietic master regulators Cdkn1a and Cebpβ upon loss of Atf7ip or Setdb1, revealing a critical coupling between HSPC cell-cycle control and myeloid differentiation. However, Atf7ip/Setdb1-mediated H3K9me3 modification does not control directly erythroid fate determination, as the levels of H3K9me3-ChIP and Setdb1-ChIP on erythroid signature/related genes were not altered in Atf7ip- and Setdb1b-deficient embryos (*SI Appendix*, Fig. S5*N*). Importantly, knockdown of *cdkn1a*, but not *cebpβ* or *rig-I*, rescued the declined HSPCs and erythrocytopenia in *atf7ip*$^{-/-}$ and *setdb1*$^{-/-}$ mutants, suggesting that Cdkn1a derepression might be the primary cause underlying the defects in HSPC expansion and erythropoiesis. The ATF7IP/SETDB1-mediated epigenetic control is also underlying human myeloid leukemia. Depletion of ATF7IP or SETDB1 in human AML cells up-regulates CDKN1A and CEBPβ, as well as TE-triggered RLR inflammatory response, leading to inhibiting leukemic cell growth and inducing myeloid differentiation. Thus, future study will focus on the concerted control mechanisms about how Atf7ip/Setdb1-mediated H3K9

trimethylation occurs in a coordinated fashion on hematopoietic regulatory genes and endogenous retroviral elements to govern normal and malignant hematopoiesis. These studies may reveal epigenetic regulations and methylation controls which will be relevant in developing epigenetic therapies for potential interventions in human leukemia or other malignancies.

Materials and Methods

Procedures and Methods. Detailed information about *atf7ip* and *setdb1b* mutants, transgenic zebrafish, WISH, double FISH and qPCR, Morpholinos, mRNA microinjection, immunoblotting, coimmunoprecipitation, EdU and TUNEL, blastula transplantation, parabiosis fusion, drug treatment, flow cytometry, cell cycle assay, cell culture, shRNA knockdown, cell proliferation, RNP electroporation, $CD34^+$ HSPCs transplantation, CFU-C assay, RNA-seq, ATAC-seq, ChIP-seq, bioinformatics analyses, confocal microscopy and statistical analyses are provided in *SI Appendix*, Materials and Methods.

Data, Materials, and Software Availability. Raw ATAC-seq, RNA-seq and ChIP-seq data data have been deposited in NCBI Sequence Read Archive database (PRJNA823899, PRJNA822693, PRJNA821990, PRJNA821630, PRJNA820962, PRJNA820605, PRJNA820309, PRJNA819547, PRJNA818304, PRJNA812352, PRJNA890767, and PRJNA890871). All other data are included in the article and/or *SI Appendix*.

ACKNOWLEDGMENTS. We thank Lili Jing for providing *Tg*(*lyz*:DsRed); Dengli Hong for providing HL-60 and OCI-AML3 cells; Samuel Wattrus (Harvard Medical School) for advice for parabiosis experiment; Haixia Jiang (Jiao Tong University) for FACS technical support; ECNU Multifunctional Platform for Innovation for image acquisition and T.P.Z. lab members for comments on the manuscript. This work was supported by grants from Ministry of Science and Technology of China (2018YFA0801004, 2018YFA0800103, 2018YFA0108700) and National Natural Science Foundation of China (NSFC31970780, NSFC31530044, NSFC81720108004).

Author affiliations: [a]Shanghai Key Laboratory of Regulatory Biology, Shanghai Frontiers Science Center of Genome Editing and Cell Therapy, Institute of Molecular Medicine, East China Normal University School of Life Sciences, Shanghai 200241, China; [b]School of Life Sciences and Technology, Tongji University, Shanghai 200092, China; [c]Guangdong Cardiovascular Institute, Guangdong Provincial People's Hospital, Guangdong Academy of Medical Sciences, Guangzhou, Guangdong 510100, China; and [d]SEU-ALLEN Joint Center, Institute for Brain and Intelligence, Southeast University, Nanjing, Jiangsu 210096, China

Author contributions: J.W., J.L., L.K., Y.W., and T.P.Z. designed research; J.W., J.L., K.C., G.L., Y.Z., W.C., and X.Z. performed research; J.W., J.L., T.T.N., B.Z., D.J., D.L., P.Z., and T.P.Z. analyzed data; and J.W., J.L., and T.P.Z. conceived the project and wrote the paper.

1. H. Ema, H. Nakauchi, Expansion of hematopoietic stem cells in the developing liver of a mouse embryo. *Blood* **95**, 2284–2288 (2000).
2. S. J. Wattrus, L. I. Zon, Stem cell safe harbor: The hematopoietic stem cell niche in zebrafish. *Blood Adv.* **2**, 3063–3069 (2018).
3. D. T. Li *et al.*, VCAM-1(+) macrophages guide the homing of HSPCs to a vascular niche. *Nature* **564**, 119–124 (2018).
4. S. Rybtsov, A. Ivanovs, S. Zhao, A. Medvinsky, Concealed expansion of immature precursors underpins acute burst of adult HSC activity in foetal liver. *Development* **143**, 1284–1289 (2016).
5. J. Y. Bertrand *et al.*, Haematopoietic stem cells derive directly from aortic endothelium during development. *Nature* **464**, 108–111 (2010).
6. S. Zhao, S. Feng, Y. Tian, Z. Wen, Hemogenic and aortic endothelium arise from a common hemogenic angioblast precursor and are specified by the Etv2 dosage. *Proc. Natl. Acad. Sci. U.S.A.* **119**, e2119051119 (2022).
7. A. Mendelson, P. S. Frenette, Hematopoietic stem cell niche maintenance during homeostasis and regeneration. *Nat. Med.* **20**, 833–846 (2014).
8. J. Xia *et al.*, A single-cell resolution developmental atlas of hematopoietic stem and progenitor cell expansion in zebrafish. *Proc. Natl. Acad. Sci. U.S.A.* **118**, e2015748118 (2021).
9. I. C. Macaulay *et al.*, Single-cell RNA-sequencing reveals a continuous spectrum of differentiation in hematopoietic cells. *Cell Rep.* **14**, 966–977 (2016).
10. L. Velten *et al.*, Human haematopoietic stem cell lineage commitment is a continuous process. *Nat. Cell Biol.* **19**, 271–281 (2017).
11. E. M. Pietras *et al.*, Functionally distinct subsets of lineage-biased multipotent progenitors control blood production in normal and regenerative conditions. *Cell Stem. Cell* **17**, 246–246 (2015).
12. F. De Graeve, A. Bahr, B. Chatton, C. Kedinger, A murine ATFa-associated factor with transcriptional repressing activity. *Oncogene* **19**, 1807–1919 (2000).
13. N. Fujita *et al.*, MCAF mediates MBD1-dependent transcriptional repression. *Mol. Cell Biol.* **23**, 2834–2843 (2003).
14. L. Liu *et al.*, MCAF1/AM is involved in Sp1-mediated maintenance of cancer-associated telomerase activity. *J. Biol. Chem.* **284**, 5165–5174 (2009).
15. T. Ichimura *et al.*, Transcriptional repression and heterochromatin formation by MBD1 and MCAF/AM family proteins. *J. Biol. Chem.* **280**, 13928–13935 (2005).
16. R. T. Timms, I. A. Tchasovnikarova, R. Antrobus, G. Dougan, P. J. Lehner, ATF7IP-mediated stabilization of the histone methyltransferase SETDB1 is essential for heterochromatin formation by the HUSH complex. *Cell Rep.* **17**, 653–659 (2016).
17. M. M. Karimi *et al.*, DNA methylation and SETDB1/H3K9me3 regulate predominantly distinct sets of genes, retroelements, and chimeric transcripts in mESCs. *Cell Stem. Cell* **8**, 676–687 (2011).
18. S. Liu *et al.*, Setdb1 is required for germline development and silencing of H3K9me3-marked endogenous retroviruses in primordial germ cells. *Gene. Dev.* **28**, 2041–2055 (2014).
19. T. Matsui *et al.*, Proviral silencing in embryonic stem cells requires the histone methyltransferase ESET. *Nature* **464**, 927–931 (2010).
20. C. F. Wang *et al.*, Reprogramming of H3K9me3-dependent heterochromatin during mammalian embryo development. *Nat. Cell Biol.* **20**, 620–631 (2018).
21. T. Tsusaka, C. Shimura, Y. Shinkai, ATF7IP regulates SETDB1 nuclear localization and increases its ubiquitination. *Embo. Rep.* **20** (2019).
22. Y. Sun *et al.*, Systematic genome editing of the genes on zebrafish Chromosome 1 by CRISPR/Cas9. *Genome. Res.* **30**, 118–126 (2019).
23. O. J. Tamplin *et al.*, Hematopoietic stem cell arrival triggers dynamic remodeling of the perivascular Niche. *Cell* **160**, 241–252 (2015).
24. S. Koide *et al.*, Setdb1 maintains hematopoietic stem and progenitor cells by restricting the ectopic activation of nonhematopoietic genes. *Blood* **128**, 638–649 (2016).
25. T. Cheng *et al.*, Hematopoietic stem cell quiescence maintained by p21cip1/waf1. *Science* **287**, 1804–1808 (2000).
26. H. Yu, Y. Z. Yuan, H. M. Shen, T. Cheng, Hematopoietic stem cell exhaustion impacted by p18(INK4C) and p21(Cip1/Waf1) in opposite manners. *Blood* **107**, 1200–1206 (2006).
27. H. Hirai *et al.*, C/EBPbeta is required for "emergency" granulopoiesis. *Nat. Immunol.* **7**, 732–739 (2006).
28. C. J. Hall *et al.*, Infection-responsive expansion of the hematopoietic stem and progenitor cell compartment in zebrafish is dependent upon inducible nitric oxide. *Cell Stem. Cell* **10**, 198–209 (2012).
29. C. J. Ceol *et al.*, The histone methyltransferase SETDB1 is recurrently amplified in melanoma and accelerates its onset. *Nature* **471**, 513–517 (2011).
30. S. M. Zhang *et al.*, KDM5B promotes immune evasion by recruiting SETDB1 to silence retroelements. *Nature* **598**, 682–687 (2021).
31. T. Clapes *et al.*, Chemotherapy-induced transposable elements activate MDA5 to enhance haematopoietic regeneration. *Nat. Cell Biol.* **23**, 704–717 (2021).
32. Y. Chernyavskaya *et al.*, Loss of DNA methylation in zebrafish embryos activates retrotransposons to trigger antiviral signaling. *Development* **144**, 2925–2939 (2017).
33. S. Lefkopoulos *et al.*, Repetitive elements trigger RIG-I-like receptor signaling that regulates the emergence of hematopoietic stem and progenitor cells. *Immunity* **53**, 934–951 (2020).
34. W. Y. Zhang *et al.*, Zscan4c activates endogenous retrovirus MERVL and cleavage embryo genes. *Nucleic. Acids. Res.* **47**, 8485–8501 (2019).
35. A. Yokota *et al.*, C/EBPbeta is a critical mediator of IFN-alpha-induced exhaustion of chronic myeloid leukemia stem cells. *Blood Adv.* **3**, 476–488 (2019).
36. P. P. Guo *et al.*, Histone variant H3.3 maintains adult haematopoietic stem cell homeostasis by enforcing chromatin adaptability. *Nat. Cell Biol.* **24**, 99–111 (2022).
37. D. M. Popescu *et al.*, Decoding human fetal liver haematopoiesis. *Nature* **574**, 365–371 (2019).
38. Y. X. Wu *et al.*, Highly efficient therapeutic gene editing of human hematopoietic stem cells. *Nat. Med.* **25**, 776–783 (2019).
39. S. Rahmig *et al.*, Improved human erythropoiesis and platelet formation in humanized NSGW41 mice. *Stem Cell Rep.* **7**, 591–601 (2016).
40. J. Jung *et al.*, CBX7 induces self-renewal of human normal and malignant hematopoietic stem and progenitor cells by canonical and non-canonical interactions. *Cell Rep.* **26**, 1906–1918 (2019).
41. C. Navarro, J. Lyu, A. M. Katsori, R. Caridha, S. J. Elsasser, An embryonic stem cell-specific heterochromatin state promotes core histone exchange in the absence of DNA accessibility. *Nat. Commun.* **11**, 5095 (2020).
42. K. Klauke *et al.*, Polycomb Cbx family members mediate the balance between haematopoietic stem cell self-renewal and differentiation. *Nat. Cell Biol.* **15**, 353–362 (2013).
43. P. Vizan *et al.*, The Polycomb-associated factor PHF19 controls hematopoietic stem cell state and differentiation. *Sci Adv.* **6**, eabb2745 (2020).
44. G. K. Griffin *et al.*, Epigenetic silencing by SETDB1 suppresses tumour intrinsic immunogenicity. *Nature* **595**, 309–314 (2021).